Nanoscale Advances

ROYAL SOCIETY OF CHEMISTRY

PAPER

View Article Online
View Journal

Cite this: DOI: 10.1039/d5na00687b

Bioorthogonal conjugation of NIR luminescent gold nanoclusters with multifunctional polymers: insights into binding efficiency, kinetics, and optical properties

Furhan Abdul Rezak, [ab] Pelin Catal,[c] Lola Mantout,[c] Fernande Da Cruz,[c] Didier Boturyn, [b] Jean-Luc Coll, [a] Arnaud Favier, [c] Galina V. Dubacheva *[b] and Xavier Le Guével *[a]

The bioorthogonal reactivity of gold nanoclusters (AuNCs) with macromolecules such as polymers is strongly influenced by their physicochemical parameters, which govern both reaction selectivity and kinetics. Using a quartz crystal microbalance with dissipation monitoring (QCM-D), we demonstrate that the strain-promoted azide–alkyne cycloaddition (SPAAC) reaction between azide-functionalized AuNCs and dibenzyl cyclooctyne (DBCO)-functionalized polymers in aqueous environments is highly specific yet proceeds at a relatively slow rate. Under diluted conditions (μM range), this reaction occurs predominantly at the level of individual nanoclusters, resulting in surface functionalization without extensive network formation. Optical characterization studies reveal a temperature- and concentration-dependent enhancement of AuNC photoluminescence upon their SPAAC conjugation with polymers. Furthermore, increased DBCO density in the polymer correlates with stronger photoluminescence enhancement, suggesting accelerated SPAAC kinetics and denser polymer coverage, consistent with the QCM-D observations. The insights gained from this work provide valuable guidance for an efficient bioorthogonal coupling between multifunctional AuNCs and polymers under biological conditions. Moreover, the developed experimental approach offers a versatile platform to investigate the formation and dynamics of various types of AuNC assemblies, including individual functional clusters and extended networks by delivering complementary information on kinetics, specificity, and luminescence properties.

Received 17th July 2025
Accepted 17th August 2025

DOI: 10.1039/d5na00687b

rsc.li/nanoscale-advances

1. Introduction

In the field of targeted medicine such as cancer therapy, the development of *in vivo* bioorthogonal reactions—pioneered by Nobel laureate Carolyn Bertozzi—marked a major breakthrough.[1] These reactions enable selective and biocompatible chemical transformations within living systems, occurring between functional groups that are absent in natural biological processes. Significant progress has since been made in controlling the kinetics and selectivity of bioorthogonal ligations notably by strain-promoted azide–alkyne cycloaddition (SPAAC) at the cancer cell surface.[2] These advances have been further propelled by the engineering of diverse reactive molecules (carbohydrates, antibodies, and peptides). Some recent reviews summarized the most efficient and safe strategies and their *in vivo* applications in therapy and diagnostics.[3–5]

In the meantime, there is the emergence of a sub-class of ultra-small luminescent gold nanoparticles called gold nanoclusters (AuNCs) for biomedical applications.[6,7] The control of their size and ligand engineering allows fine-tuning of their photoluminescence properties, notably in the near infrared (NIR) for *in vivo* imaging,[6,8–11] as well as their pharmacokinetics, including high renal clearance,[12–14] and enables the introduction of targeting modalities.[15,16] In addition, their activation by light and X-rays at targeted sites has shown promise for cancer therapy.[17–21] A key feature of AuNCs is the ability to functionalize their surface with specific ligands, while using their optical properties as a read out of the local environment.[22] On the other hand, conjugation of AuNC assemblies with synthetic and natural polymers and polymeric assemblies has opened a new library of biocompatible AuNCs with unique optical properties, improved stability and controlled functionality.[23–26]

To date, few studies have explored the functionalization of AuNCs with SPAAC reactive groups. For instance, NMR

[a]Université Grenoble Alpes, Institut pour l'Avancée des Biosciences (IAB)INSERM U1209, CNRS-UMR 5309, 38700 Grenoble, France. E-mail: xavier.le-guevel@univ-grenoble-alpes.fr

[b]Université Grenoble Alpes, Département de Chimie Moléculaire (DCM)CNRS-UMR 5250, 38000 Grenoble Cedex 9, France. E-mail: galina.dubacheva@univ-grenoble-alpes.fr

[c]Universite Claude Bernard Lyon 1, INSA Lyon, Université Jean Monnet, CNRS UMR 5223, Ingénierie des Matériaux Polymères, F-69621 Villeurbanne, France

spectroscopy confirmed the successful conjugation of alkyne-fluorescein to ultra-small gold nanoparticles (<2 nm) displaying azide groups.[27] Another noticeable example demonstrated the high SPAAC reactivity of the atomically precise $Au_{25}(SCH_2CH_2$-*p*-C_6H_4-$N_3)_{18}$ with strained cyclooctyne, supported by comprehensive structural and spectroscopic analyses.[28]

Despite these advances, the SPAAC functionalization of AuNCs with macromolecules, such as functional polymers bearing dibenzocyclooctyne (DBCO) or bicyclononyne (BCN) groups, remains largely unexplored. Nonetheless, biocompatible DBCO-functionalized polymers exhibit a strong potential for *in vivo* click chemistry, especially if they are based on multifunctional polymer chains synthesized by RAFT-controlled radical polymerization that are characterized by a precisely tunable molecular weight and composition. Indeed, the latter can be used to produce water-soluble and biocompatible polymer chains that can incorporate multiple functionalities, like various types of ligands, fluorophores or other imaging reporters and biotargeting entities.[29] Furthermore, such polymers are known to passively accumulate in tumors following injection *in vivo* thanks to the EPR effect.[29] In this context, the modular synthetic platform based on well-defined linear P(NAM-stat-NAS) (poly(*N*-acryloylmorpholine-stat-*N*-acryloxysuccinimide)) copolymers synthesized by RAFT polymerization is of particular interest.[30] These polymer chains, with an azeotropic composition of 60 mol% NAM and 40 mol% NAS, bear regularly spaced activated esters, allowing the introduction of a controlled number of bioorthogonal groups such as DBCO for SPAAC. It is thus possible to vary both the molecular weight and the DBCO density of the polymer chains.

This study aims to deepen the understanding of the SPAAC reaction between azide-functionalized, NIR-emitting AuNCs and tunable biocompatible polymers bearing DBCO groups (Scheme 1). A systematic experimental approach, combining complementary physico-chemical techniques, including a quartz crystal microbalance with dissipation monitoring (QCM-D) and photoluminescence spectroscopy, was employed to investigate key aspects of the SPAAC conjugation process, such as specificity, binding kinetics and optical properties of the resulting nanoconjugates.

2. Materials and methods

2.1. Materials

N,*N*-Diisopropylethylamine (DIPEA, ≥99,5%), dibenzylcyclooctyne-amine (DBCO-NH_2), amino propanediol (APD), diethyl ether (Et_2O, ≥99.5%), tetrachloroauric(III) acid trihydrate ($HAuCl_4 \cdot 3H_2O$, 99.9%), sodium borohydride ($NaBH_4$, 99%), sodium hydroxide (NaOH), streptavidin (SAv, $M_w = 60$ kg mol^{-1}), biotin-EG_{12}-DBCO (EG: ethylene glycol, $M_w = 1102$ g mol^{-1}), organic solvents (DMSO, DMF, $CHCl_3$ *etc.*), and deuterated water were purchased from Sigma-Aldrich. Anhydrous *N*,*N*-dimethylformamide (DMF, 99.8%) was purchased from Acros Organics. LA-$PEGN_3$ ($M_w = 400$ g mol^{-1}) and LA-$PEGOCH_3$ ($M_w = 750$ g mol^{-1}) (LA: lipoic acid, PEG: polyethylene glycol) were purchased from Interchim. HS-$(CH_2)_{11}$-EG_6-Biotin ($M_w = 694$ g mol^{-1}) and HS-$(CH_2)_{11}$-EG_4-OH ($M_w = 380.06$ g mol^{-1}) were purchased from Prochimia. PBS (10 mM, pH 7.1, with Ca^{2+}, Mg^{2+}, K^+ and Na^+ ions) and DMEM (pH 7.2, with glucose, L-glutamine, HEPES, phenol red free, supplemented with 10% FBS) buffers were purchased from Thermo Fischer. NaCl_HEPES buffer was made using 10 mM HEPES, 150 mM NaCl and adjusted to pH 7.4. Ultrapure deionized water (resistivity 18.2 MΩ cm) was used for all experiments.

2.2. Synthesis of polymer chains displaying DBCO groups

Multifunctional polymers were prepared from reactive copolymer precursors based on *N*-acryloylmorpholine (NAM) and *N*-acryloxysuccinimide (NAS) P(NAM-stat-NAS) that were synthesized by RAFT polymerization following a previously reported procedure.[14] Two P(NAM-stat-NAS) precursor backbones with respectively $M_n = 18.6$ and 91.7 kg mol^{-1}, as determined by SEC-MALLS, were functionalized to present different densities of DBCO lateral groups (Table S1). Polymers were named according to the molecular weight of the starting polymer backbone, followed by the rounded average number of DBCOs per polymer chain.

Typically, for the 19K-12DBCO polymer (*i.e.* precursor backbone $M_n = 18.6$ kg mol^{-1}, 12 DBCOs per chain), P(NAM-stat-NAS) copolymer ($M_n = 18.6$ kg mol^{-1}; $Đ = 1.09$; 1.34 μmol; 1 eq.) was dissolved in anhydrous DMF (1 mL). A solution of DBCO-NH_2 (17 μmol; 12.63 eq.) in anhydrous DMF (250 μL) was then added, along with DIPEA (68 μmol). The reaction medium was stirred for 2 hours at room temperature, protected from light, before the polymer was precipitated in cold diethyl ether and dried under vacuum. After re-solubilization in DMF, 10 mL of borate buffer (0.5 M, pH 8) was added for hydrolysis of the remaining activated ester groups. The mixture was stirred for 24 hours before addition of APD (6.7 μmol) and stirred for another 24 hours. The resulting polymer was purified by ultrafiltration (10 kDa MWCO; Millipore Amicon) against deionized water and then recovered by freeze-drying. Other polymers were synthesized following the same procedure by adjusting the molecular weight of the starting polymer as well as the DBCO-NH_2 stoichiometry and characterized by ^{1}H NMR (Fig. S1–S3).

2.3. Synthesis of AuNCs functionalized with azide groups

The AuNCs were synthesised by the sodium borohydride reduction of the tetrachloroauric(III) salt in the presence of LA-$PEGN_3$ or LA-$PEGOCH_3$ ligands as reported.[31] Briefly, 12 mg of LA-$PEGN_3$ (3×10^{-5} mol, 3 eq.) or 21 mg of LA-$PEGOCH_3$ (3×10^{-5} mol, 3 eq.) was dissolved in 10 mL of water and stirred at 350 rpm at room temperature before adding 100 μL NaOH (1 M). Following this, 200 μL $HAuCl_4$ (1×10^{-5} mol, 1 eq.) was added corresponding to a molar ratio of Au : ligand = 1 : 3 and stirred for 5 minutes. 200 μL of freshly prepared $NaBH_4$ (2×10^{-5} mol, 2 eq.) was added dropwise to the mixture under vigorous stirring. The solution changed from yellowish to light brown immediately after the addition of the reducing agent. The mixture was then stirred for 16 hours at room temperature. The solution was then purified to remove free ligands by four cycles of centrifugation/filtration using a 3 kDa ultra centrifuge

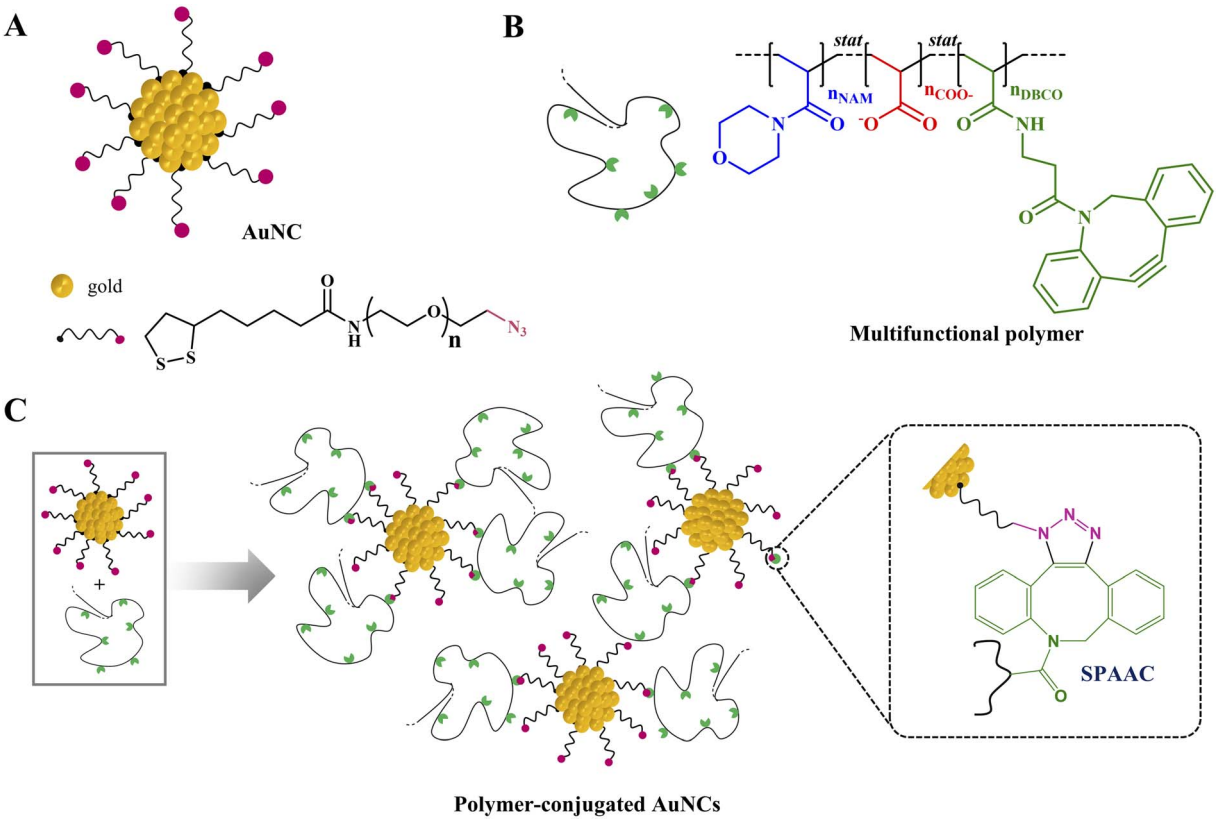

Scheme 1 Schematic representation of SPAAC conjugation between AuNCs and multifunctional polymers: (A) AuNCs stabilized with LA-PEGN$_3$ (LA: lipoic acid, PEG: polyethylene glycol, average number of PEG units, $n = 4–6$), (B) structure of DBCO-functionalized polymer chains (NAM: *N*-acryloylmorpholine), and (C) SPAAC reaction between azide-functionalized AuNCs and DBCO-bearing polymers.

filter (Amicon, UFC9003). The resulting solution was stored at 4 °C until further use. The obtained Au-PEGN$_3$ and Au-PEGOCH$_3$ nanoclusters, stabilised with LA-PEGN$_3$ and LA-PEGOCH$_3$, respectively, were characterized by ^{1}H NMR, ^{1}H DOSY NMR, TEM, MALDI-Tof, PAGE, FT-IR, absorbance and fluorescence spectroscopy.

2.4. Conjugation of AuNCs with polymers

The conjugation was performed by the subsequent addition of polymer and nanocluster stock solutions (103 and 71 μM, respectively, both prepared in water) to PBS. The volumes of stock solutions were adjusted to tune the polymer : AuNC molar ratio in the range from 10 : 1 to 1 : 10 which corresponds to the final polymer and nanocluster concentrations varied in the range from 1 to 20 μM and from 1 to 40 μM, respectively. In a typical experiment with the polymer : AuNC molar ratio equal to 10 : 1 (at 10 μM polymer concentration), 117.2 μL of polymer stock solution (103 μM) was added to 1.07 mL of PBS. This mixture was sonicated for 3 minutes to ensure uniform dispersion of the polymer. Subsequently, 16.8 μL of Au-PEGN$_3$ (71 μM) was added dropwise to the polymer solution. The resulting mixture was vortexed briefly and kept undisturbed for prescribed times (5, 10, 30, 60, and 90 minutes). In addition to the polymer : AuNC ratio, several parameters were tuned including polymer characteristics (molecular weight and DBCO density), temperature (25 or 37 °C) and medium (PBS or DMEM with 10% serum).

2.5. Transmission electron microscopy (TEM)

Metal core sizes of AuNCs were characterized using a JOEL JEM 2100 Plus TEM at an accelerating voltage of 200 kV. The samples were prepared by drop-casting AuNC dispersion onto a carbon-coated copper grid, followed by rinsing to remove salts present in the buffer and drying. The average particle sizes estimated on at least 200 nanoclusters were determined using ImageJ software.

2.6. Nuclear magnetic resonance (NMR)

The ^{1}H NMR and ^{1}H DOSY NMR experiments were performed using a Bruker AVANCE III spectrometer operating at 400.13 MHz using deuterated PBS. A 5 mm Z-gradients BBIDiff probe was used for ^{1}H DOSY experiments. The standard LEDBPGP2S pulse Bruker sequence is used to acquire the ^{1}H DOSY spectra. The gradient pulse duration (δ) was individually optimized for each sample, ranging from 1000 to 5000 μs. A diffusion delay of 100 ms was used. In all experiments, gradient strengths were linearly incremented from 5.266 to 157.973 G cm^{-1} over 30 steps, employing smooth square-shaped pulses (SMSQ10.100). Each measurement consisted of sixty-four scans. Free induction decays (FIDs) were processed using Fourier transformation with

a 2 Hz Lorentzian line broadening, applying automatic baseline correction in TopSpin software (Bruker). The experimental signal amplitude (I) as a function of gradient strength for a single component is described by the Stejskal–Tanner equation[24]

$$I = I_o e^{-D\gamma^2 g^2 \delta^2 \left(\Delta - \frac{\delta}{3} - \frac{\tau}{2}\right)}$$

where, I_o is the amplitude at zero gradient (reference amplitude), D is the diffusion coefficient, γ is the gyromagnetic ratio of the nucleus under observation, g is the gradient strength, δ is the gradient pulse length and Δ is the diffusion time. Depending on the number of components contributing to the signal and on the dispersity of the samples the values of diffusion coefficients can be extracted by mono, multi-exponential or Inverse Laplace Transform fitting of the curves. ILT was preferred here and Dynamic Center software (Bruker) was used for processing. The D is related to the hydrodynamic diameter (R_H) by the Stokes–Einstein equation (assuming molecules as spherical):

$$R_H = \frac{k_B T}{3D\pi\eta}$$

where k_B is the Boltzmann constant, T is the temperature and η is the viscosity of the solvent (here, we assumed the $\eta_{d\ PBS}$ to be the same as $\eta_{D_2O} = 1.232 \times 10^{-3}$ Pa s at 298 K).[32]

2.7. Matrix-assisted laser desorption ionization–time of flight (MALDI-tof)

The average molecular weight of the AuNCs was determined by MALDI-tof in positive mode using an Autoflex Speed mass spectrometer (Bruker Daltonics). Samples were prepared by dissolving the nanoclusters in water in the concentration range of 0.25–0.50 g L^{-1}. α-Cyano-4-hydroxycinnamic acid (HCCA) dissolved in TA30 (water/acetonitrile; 70/30 v/v with 0.1% trifluoroacetic acid) was used as a matrix. Matrix and sample solutions were mixed at a 1 : 1 v/v ratio in water. 1 μL of the mixture was deposited onto the MALDI sample plate and dried, followed by the MALDI-tof analysis.

2.8. Fourier transform infrared (FT-IR) spectroscopy

The FT-IR spectra of freeze-dried AuNCs were collected on a Thermo Scientific Nicolet iS10 spectrometer in the range from 600 to 4000 cm^{-1} with an average of 32 scans for each spectrum. A blank spectrum was measured in air and subtracted from all sample spectra to eliminate atmospheric contributions.

2.9. Absorption and emission spectroscopies

Absorbance spectra were recorded on a ThermoScientific Evolution 201 UV-visible spectrophotometer. The baseline recorded for solvent alone was subtracted from all absorbance spectra. The photoluminescence (PL) spectra of AuNCs and polymers conjugated to AuNCs were recorded on a Horiba Fluoromax-4 spectrofluorometer between 470 and 850 nm while exciting at 450 nm wavelength and on an FLS-1000 Edinburgh Instrument equipped with an InGaAs detector between 850 and 1400 nm while exciting at other wavelengths (550, 690 and 780 nm). The excitation spectra were recorded in the range from 350 to 900 nm at the emission wavelength of 1000 nm. The fluorescence signal was corrected by removing the wavelength sensitivity of detectors. In addition, the reference detector was used to remove the temporary fluctuations caused by the lamp. To determine the PL emission enhancement, two parallel samples were prepared and measured: AuNCs alone and polymer-conjugated AuNCs. The emission spectra were recorded for both sets at identical time intervals, and at each time point, the PL enhancement was calculated as the ratio of the integrated area under the emission curve of the conjugated AuNCs to that of the AuNCs alone. The area under the emission curves was calculated using Origin Pro software. Measurements were performed with 300 μL of samples at 20 °C in a quartz cuvette (optical path length = 1 cm).

2.10. Polyacrylamide gel electrophoresis (PAGE)

For PAGE experiments, stacking and separating gels were prepared from 25.0 wt% acrylamide and 2.5 wt% bis-acrylamide, respectively. The eluting buffer was a mixture of glycine (14.4 g) and tris(hydroxymethyl)aminoethane (3.0 g) dissolved in 100 mL of water and adjusted to pH 7. After adding 1 μL glycerol per 10 μL of AuNCs (4 g L^{-1}), the samples were loaded into the wells of the stacking gel (10 μL per well). The electrophoresis was performed at a constant voltage of 130 V using a Mini PROTEAN Bio-Rad (Hercules, CA, USA) for 2 hours. The AuNCs were then detected by NIR-II imaging.

2.11. NIR-II imaging

NIR-II imaging was performed using a NIR-II Princeton camera 640ST (900–1700 nm) coupled with a laser excitation source of 808 nm (120 mW cm^2). A short-pass excitation filter (at 1000 nm, Thorlabs) and a long-pass emission filter (at 1064 nm, Semrock) coupled with a 50 mm lens (Navitar) with a numerical aperture of 4 were used.

2.12. Quartz crystal microbalance with dissipation monitoring (QCM-D)

Specificity, kinetics and stoichiometry of click conjugation were studied on surfaces using a QCM-D. QCM-D measurements were performed with a Q-Sense E4 system equipped with Q-Sense flow Modules (Biolin Scientific) on gold-coated quartz crystals (Quartz Pro). The flow rate was fixed to 20 μL min^{-1} using a peristaltic pump (Ismatec, IPC 4). The shifts in frequency (Δf) and dissipation (ΔD) were recorded at 24 °C, except for the experiment to evaluate the effect of temperature (37 °C). The QCM-D data were collected for six overtones ($i = 3$, 5, 7, 9, 11 and 13) along with the fundamental resonance frequency (4.95 MHz) using QTools software. The changes in Δf and ΔD of the fifth overtone ($i = 7$) are presented; all other overtones would have provided qualitatively equivalent information.

To study the click reaction on surfaces, gold-coated QCM-D sensors were functionalized with DBCO groups as follows. First, biotinylated self-assembled monolayers (b-SAMs) were

formed on gold surfaces *ex situ* following a previously developed protocol.[33,34] Briefly, the gold surface was rinsed with water, dried with an air gun and exposed to UV-ozone treatment (20 min). The surface was then immersed in a mixture of HS-$(CH_2)_{11}$-EG_6-biotin and HS-$(CH_2)_{11}$-EG_4-OH thiols at a 1 : 9 ratio (1 mM total concentration) in ethanol overnight. Next day, the functionalized surfaces were rinsed with ethanol to remove excess thiols and dried. The gold crystals were then mounted to QCM-D chambers and exposed to a flow of NaCl_HEPES buffer. After obtaining a stable baseline, streptavidin (SAv, 10 μg.mL^{-1} in NaCl_HEPES buffer), followed by biotin-EG_{12}-DBCO (20 μg.mL^{-1} in NaCl_HEPES buffer), was injected to generate the DBCO monolayer. After rinsing with NaCl_HEPES buffer, the running medium was changed to PBS and the functionalized surface was exposed to (i) Au-$PEGN_3$ or Au-$PEGOCH_3$ (1 μM) followed by the injection of polymers (10 μM) displaying DBCO or (ii) to polymer : cluster mixtures at different ratios.

3. Results and discussion

We conducted a systematic study to investigate the efficiency of bioorthogonal click conjugation between AuNCs and multifunctional polymers and how it was affected by different parameters including the polymer : AuNC ratio, polymer molecular weight and DBCO density, temperature, reaction medium and reaction time. After characterization of the synthesized polymers and AuNCs, we used a QCM-D to evaluate the specificity, stoichiometry and kinetics of their SPAAC conjugation with polymers. Then, the optical properties of the obtained conjugates were evaluated using UV-visible and photoluminescence spectroscopy, providing further insights to the kinetics and efficiency of the click reaction.

3.1. Characterisation of multifunctional polymers

To study the influence of the polymer chain molecular weight and DBCO density on SPAAC conjugation, two P(NAM-stat-NAS) reactive precursors with M_n = 18.6 and 91.7 kg mol^{-1} were synthesized by a RAFT-controlled radical polymerization and characterized by ^{1}H NMR (see Materials and methods, Fig. S1). These precursors were then reacted with various amounts of a DBCO amino-derivative (DBCO-NH_2) and the coupling yield was determined by ^{1}H NMR (Fig. S2). The very efficient DBCO coupling onto the polymer was clearly evidenced by the appearance of broad peaks at 5.1 and 7–8 ppm, corresponding respectively to one of the –CH_2- protons of the cyclooctyne and to the aromatic protons of the DBCO group. This allowed determination of the average number of DBCO units per polymer chain (n_{DBCO}) (Table 1). After hydrolysis of the remaining activated esters, terpolymers presenting NAM, DBCO-functionalized and acrylic acid units were obtained (Scheme 1). Importantly, although DBCO units are quite hydrophobic, the resulting polymer chains were water-soluble within the studied DBCO density range, thanks to the predominance of negatively-charged carboxylate groups from acrylic acid units. Details of the synthesized polymers, including abbreviation, DBCO density, and molecular weight are provided in Table 1.

Table 1 List of polymers used with respective numbers of DBCO and COO^- units per polymer chain and molecular weights

Polymer name	n_{DBCO}	n_{COO^-}	M_n (kg mol^{-1})
19K-0DBCO	0	48.3	13.8
19K-12DBCO	12.1	36.2	16.6
19K-24DBCO	24.2	24.1	20.0
92K-0DBCO	0	239.8	68.2
92K-46DBCO	45.7	194.1	80.0
92K-93DBCO	92.9	146.9	92.2

The final polymers were also analysed by ^{1}H NMR in deuterated PBS (Fig. S3) and the accessibility and reactivity of the DBCO groups for SPAAC in aqueous media were further confirmed by coupling tests with an azido fluorescent dye, AlexaFluor 647 (AF647-N_3), in PBS. Indeed, size-exclusion chromatography with UV-vis detection (SEC-UV) demonstrated that SPAAC coupling yield was >80% after 2 hours (Fig. S4).

3.2. Physico-chemical characterisation of AuNCs

The structural properties of Au-$PEGN_3$ nanoclusters were characterized by TEM, NMR, MS, PAGE and FT-IR. HR-TEM characterization showed that Au-$PEGN_3$ nanoclusters have an average metal core size of 2.1 ± 0.4 nm (Fig. 1A and Table 2). The average diffusion coefficient of Au-$PEGN_3$ nanoclusters, as determined by DOSY NMR was (5.9 ± 0.2) × 10^{-11} m^2 s^{-1} (Fig. 1B), corresponding to a hydrodynamic diameter of 3.0 ± 0.2 nm (Table 2). Mass spectra indicated a molar mass particle distribution M_w = 6–10 kg mol^{-1}, dominated by the polydispersity in number of gold atoms[32] (Fig. S5, Table 2). PAGE is a technique that is used to separate molecules based on their size and charge, allowing the characterization of molecular weight and purity, and this technique further confirmed a relatively broad size distribution of Au-$PEGN_3$ (Fig. S6A). The presence of azide groups in Au-$PEGN_3$ was confirmed from the FT-IR spectrum showing the band at 2135 cm^{-1}, consistent with values reported in the literature[31] (Fig. 1C and Table S1). In comparison to the free ligand, the ^{1}H NMR spectrum of the Au-$PEGN_3$ nanoclusters exhibited significantly broadened peaks (with a small chemical shift and loss of multiplicity), indicating that the ligands were indeed in interaction with the gold surface and not free in solution (Section S2.1).

The optical properties of Au-$PEGN_3$ nanoclusters were further characterized by UV-visible absorbance and photoluminescence spectroscopy. The characterization of Au-$PEGN_3$ reveals a typical absorbance profile of AuNCs with weakly defined absorption shoulders at 520 and 700 nm[35] (consistent with the excitation spectra, Fig. S6B), which could be attributed to the inter- and intra-electronic transitions in the metal core and between the metal surface and the ligands.[36] Photoluminescence emission spectra display a large Stokes shift and a NIR signal, with a broad emission band centered at 789 nm when excited at 450 nm (Fig. 1D), as previously reported for pegylated AuNCs.[37,38] The PL emission profile of Au-$PEGN_3$ (1 μM) remains stable over time (90 min) in PBS (Fig. S6C). These nanoclusters also emit in the NIR-II region with

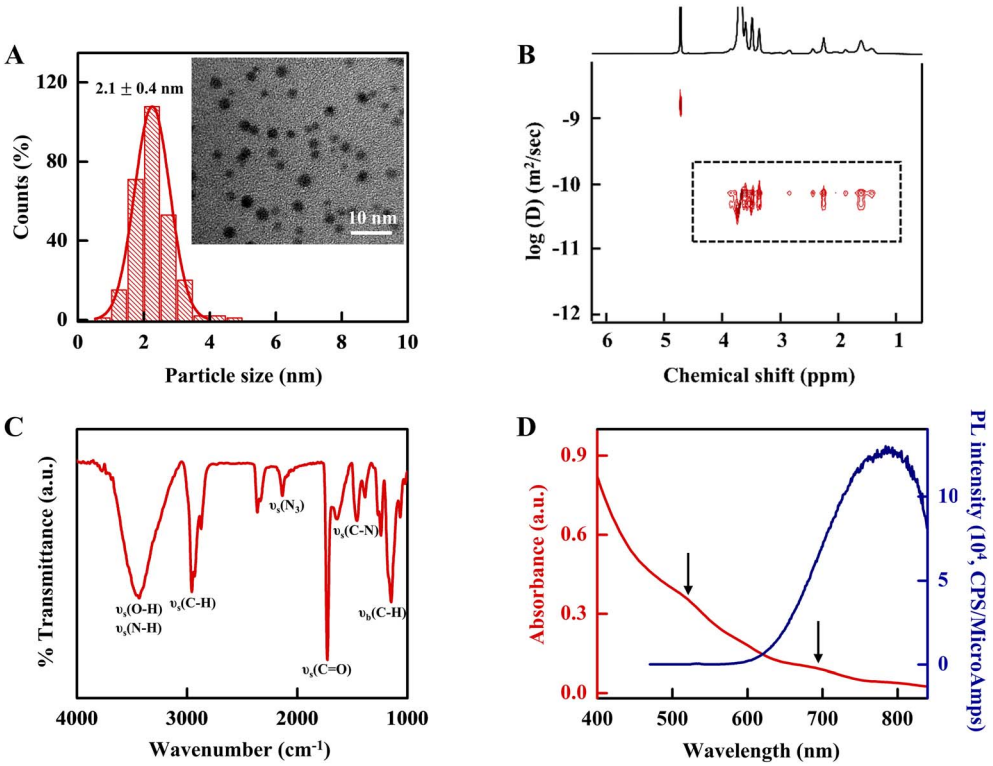

Fig. 1 Characterization of Au-PEGN$_3$ nanoclusters. (A) The characteristic TEM image and average particle size distribution of Au-PEGN$_3$ from TEM analysis using 274 particles. (B) ^{1}H-DOSY NMR of Au-PEGN$_3$ (30 μM) dispersed in deuterated PBS at 298 K, plotted as log(diffusion coefficient, *D*) *vs.* ^{1}H NMR chemical shifts associated with specific protons of the ligands. The average *D* of water molecules in the sample is 1.66 × 10^{-9} m^2 s^{-1} and that of Au-PEGN$_3$ is represented inside the black dotted rectangle with a mean value of 5.9 × 10^{-11} m^2 s^{-1}. The measured *D* value reflects the translational mobility of Au-PEGN$_3$ and was used to calculate the hydrodynamic diameter (see Table 1). (C) The FT-IR spectra of Au-PEGN$_3$ with characteristic shifts of 3436 cm^{-1} (O–H/N–H stretching), 2969 cm^{-1} (C–H stretching), 2135 cm^{-1} (N$_3$ stretching), 1721 cm^{-1} (C=O stretching), 1458 cm^{-1} (C–N stretching) and 1234 cm^{-1} (C–H in-plane bending). (D) Absorbance (red) and emission spectra ($\lambda_{exc.}$ = 450 nm, blue) of Au-PEGN$_3$ (1 μM) in PBS. The arrows (around 520 and 700 nm) indicate the characteristic absorption bands of Au-PEGN$_3$.

photoluminescence up to 1300 nm upon both visible and infrared excitations (Fig. S6B and D).

For control experiments, nanoclusters were synthesized with methoxy-terminated LA-PEG ligands (Au-PEGOCH$_3$) and subjected to a similar set of characterization studies. These nanoclusters exhibited a slightly smaller size compared to Au-PEGN$_3$, which is confirmed by TEM and DOSY NMR analysis (Fig. S7 and Table 2). Mass spectrometry revealed similar polydispersity in molecular weight distribution for the AuNCs, ranging from 6 to 11 kg mol^{-1} (Fig. S8 and Table 2). As expected, in contrast to Au-PEGN$_3$, the azide peak was not observed in the FT-IR spectrum of Au-PEGOCH$_3$ (Fig. S9A). Au-PEGOCH$_3$ displayed optical properties comparable to those of Au-PEGN$_3$, including emission in both the NIR-I and NIR-II regions (Fig. S9B–D).

3.3. Efficiency of nanocluster/polymer conjugation

We used a QCM-D to characterize specificity, stoichiometry and kinetics of bioorthogonal conjugation between Au-PEGN$_3$ nanoclusters and polymers displaying DBCO. In order to attach Au-PEGN$_3$ nanoclusters, the planar gold surface was functionalized with a DBCO layer in several steps described in the Materials and Methods section and summarized in Fig. S10A. Mixed biotinylated SAMs having EG chains at their extremity

Table 2 Table summarising the physicochemical parameters of Au-PEGN$_3$ and Au-PEGOCH$_3$ nanoclusters with the core size, hydrodynamic diameter and average molecular weight determined from TEM, NMR DOSY and MALDI-MS analyses, respectively. Examples of TEM and DOSY data are shown in Fig. 1, and MALDI-MS is shown in Fig. S5

	Core size (nm)	Hydrodynamic diameter (nm)	Molecular weight (kg mol^{-1})
Cluster	TEM	DOSY	MALDI-MS
Au-PEGN$_3$	2.1 ± 0.4	3.0 ± 0.2	6–10
Au-PEGOCH$_3$	1.8 ± 0.5	2.6 ± 0.2	6–11

(Fig. S10B) were used to suppress non-specific binding to the surfaces,[33] while streptavidin chemistry allowed formation of well-organized and oriented to the solution DBCO layer.[39] The synthesis of biotinylated SAMs was performed *ex situ* using previously established protocols.[34] The formation of the SAv monolayer and the subsequent attachment of biotin-EG_{12}-DBCO (Fig. S10C) was monitored *in situ* using a QCM-D. As shown in Fig. S10D, SAv rapidly binds to saturation when exposed to 10% biotinylated SAMs. The response is characterized by a frequency shift of -23.0 ± 1.5 Hz and a negligible shift in dissipation, indicating the formation of dense and rigid protein monolayers, in agreement with previous reports.[34] The subsequent injection of biotin-EG_{12}-DBCO results in an additional frequency shift of -1.4 ± 1 Hz. As quantified in previous studies,[34] an average of 1.8 biotin-binding sites remain available per SAv attached under these specific conditions (biotin fraction in SAM, SAv concentration, incubation time, buffer, *etc.*), indicating that approximately two DBCO ligands are attached to each SAv in the resulting monolayer. The specificity of binding to SAMs was evaluated using SAMs without biotin, *i.e.* made of 100% HS-$(CH_2)_{11}$-EG_4-OH. As expected, none of the building blocks (SAv, biotin-EG_{12}-DBCO, Au-$PEGN_3$ or 19K-12DBCO) bound to the SAMs lacking biotin, confirming the absence of non-specific interactions (Fig. S11).

To access the specificity of bioorthogonal conjugation, the DBCO-functionalized layer was exposed to Au-$PEGN_3$ nanoclusters. These rapidly bound to saturation, resulting in a frequency shift of $\Delta f = -10.0 \pm 1.5$ Hz (Fig. 2). The small change in dissipation ($\Delta D = 0.8 \pm 0.5 \times 10^{-6}$) indicates the formation of rigid monolayers. This Au-$PEGN_3$ monolayer was subsequently exposed to two types of polymers: 19K-0DBCO (without DBCO) and 19K-12DBCO (with 12 DBCOs on average per chain). Upon injection of 19K-0DBCO, no detectable change in frequency and dissipation was observed, confirming the absence of non-specific interactions between the polymer and Au-$PEGN_3$. In contrast, the injection of 19K-12DBCO produced a frequency shift of -9.0 ± 1.3 Hz, indicating effective binding due to the presence of DBCO moieties. The negligible dissipation shift suggests a relatively collapsed conformation, likely due to the hydrophobic nature of DBCO groups. Similar behavior was observed for the higher molecular weight polymer 92K-46DBCO (with 46 DBCOs), at a comparable DBCO density

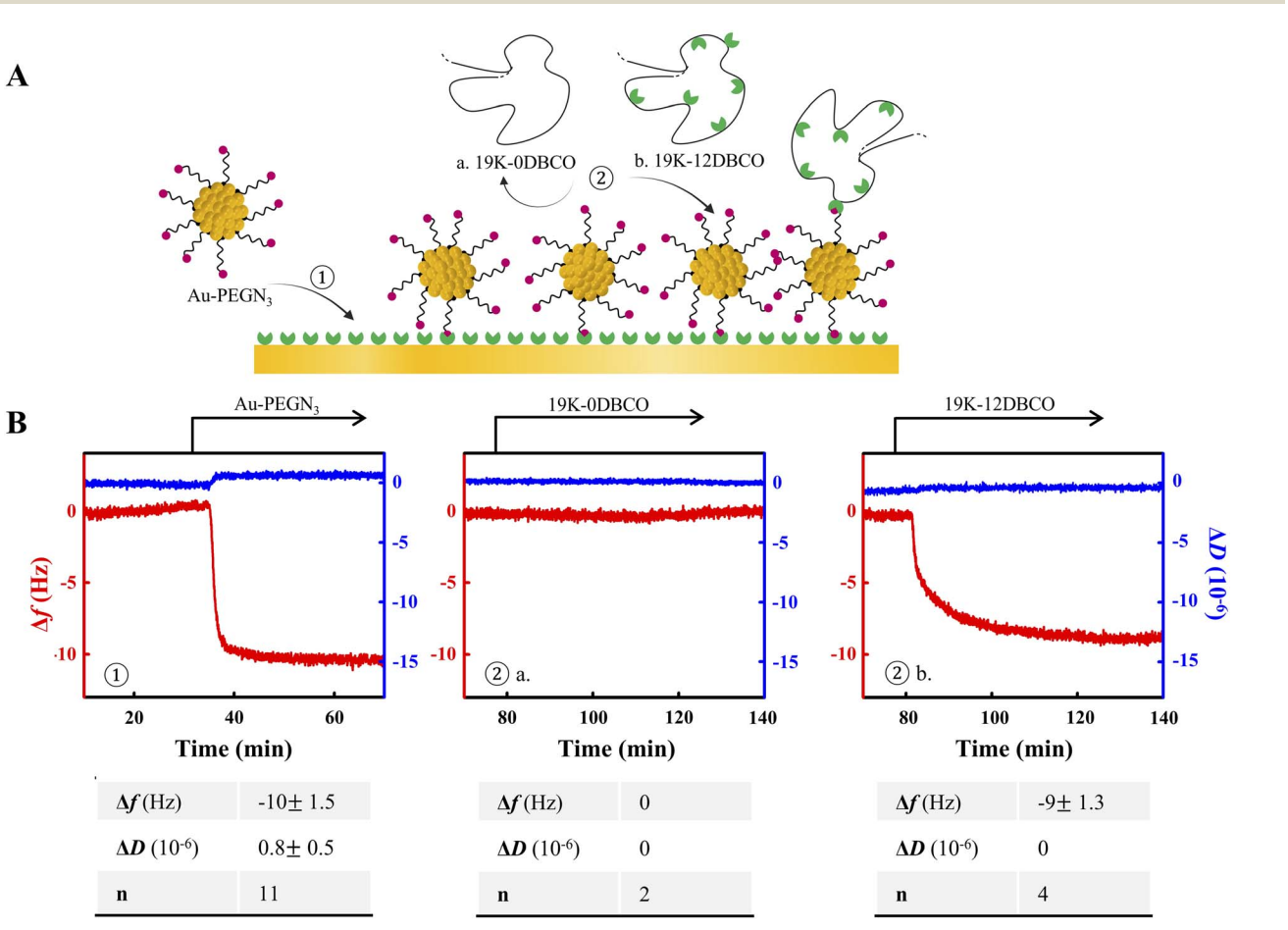

Δf (Hz)	-10± 1.5	Δf (Hz)	0	Δf (Hz)	-9± 1.3
ΔD (10^{-6})	0.8± 0.5	ΔD (10^{-6})	0	ΔD (10^{-6})	0
n	11	n	2	n	4

Fig. 2 QCM-D characterization of the specificity of bioorthogonal conjugation. (A) Schematic of the subsequent addition of ① Au-$PEGN_3$ (1 μM) and ② a. 19K-0DBCO (10 μM) or b. 19K-12DBCO (10 μM) to the surface functionalized with DBCO. (B) Representative QCM-D responses together with the tables summarizing Δf (red) and ΔD (blue) shifts determined after rinsing. Values are shown as mean ± SEM determined from *n* measurements. The arrows at the top of the QCM-D profile indicate the start and incubation duration with each sample as specified, with PBS being flushed over the sensor surface during the remaining periods.

per chain (Fig. S12). Additional control experiments confirmed the specificity of interactions: neither Au-PEGN$_3$ nor 19K-12DBCO bound to surfaces lacking DBCO (Fig. S13A). Similarly, Au-PEGOCH$_3$ nanoclusters (lacking azide groups) and 19K-12DBCO showed no binding to surfaces presenting DBCO (Fig. S13B and C). Together, these findings confirm the high specificity of the SPAAC reaction between Au-PEGN$_3$ nanoclusters and DBCO-functionalized polymers.

3.4. Stoichiometry and kinetics of nanocluster/polymer conjugation

To investigate the stoichiometry of bioorthogonal conjugation, *i.e.*, to determine the extent of the AuNC azide groups involved in conjugation, the DBCO-coated surface was exposed to mixtures of 19K-12DBCO and Au-PEGN$_3$ pre-incubated at a 10 : 1 molar ratio for one hour (at concentrations of 10 and 1 μM, respectively, Fig. 3A). The binding kinetics of these conjugates to the DBCO surface were slower than those of Au-PEGN$_3$ alone (Fig. 3B). It showed that, under these diluted conditions, some azide reactive groups are still accessible at the AuNC surface after the incubation time, although there is an excess of polymer DBCOs. Considering that SPAAC conjugation on model surfaces is specific (Fig. 2, S11–S13), polymer attachment resulted in a partial occupation and a reduced accessibility of the cluster azides, leading to the reduced binding rate. Subsequent exposure of the immobilized conjugates to additional polymer resulted in lower binding than that observed for an Au-PEGN$_3$ monolayer ($\Delta f = -3.0 \pm 1$ Hz, Fig. 3A), confirming the reduced availability of azide moieties due to prior polymer attachment. Similar trends were observed for higher molecular weight polymers, such as 92K-46DBCO (92 kg mol^{-1}, 46 DBCO per polymer, Fig. S14), supporting the conclusion that the SPAAC reaction occurs between Au-PEGN$_3$ and DBCO-bearing polymers. Interestingly, regardless of whether the polymers (19K-12DBCO : Au-PEGN$_3$ molar ratio = 10 : 1, Fig. 3) or the nanoclusters (or 19K-12DBCO : Au-PEGN$_3$ molar ratio = 1 : 8, Fig. S15) were in excess, the final frequency and dissipation shifts after ∼1 hour of incubation were similar and closely matched those obtained with pure Au-PEGN$_3$ nanoclusters under similar conditions. Additional experiments with 19K-24DBCO polymers (higher DBCO density) reinforced these findings, showing slower binding kinetics (consistent with higher azide occupancy) but similar final QCM-D shifts (Fig. 3B). These results suggest that, under the studied conditions, the SPAAC reaction leads predominantly to the functionalization of individual nanoclusters, as schematized in Fig. 3A, rather than the formation of extended nanocluster networks. Indeed, if extensive 3D assemblies were formed, significantly larger QCM-D shifts would be expected compared to those measured for monolayer binding.

Regarding conjugation kinetics, the fact that additional polymer binding is still possible after one hour of pre-incubation (despite polymer excess) indicates that the SPAAC reaction proceeds relatively slowly at those concentrations (Fig. 3A). To quantify this, we varied the pre-incubation time of Au-PEGN$_3$ and 19K-12DBCO mixtures (0–60 minutes), while keeping other parameters the same (concentrations of polymer and AuNCs are 10 and 1 μM, respectively) and then immobilized the resulting conjugates on the DBCO-coated surface. Subsequent exposure to additional polymer allowed assessment of residual binding capacity. Experiments conducted at 24 and 37 °C (Fig. 3C) showed a clear decrease in additional binding with increased pre-incubation time, confirming the slow kinetics.

One possible explanation for the slow kinetics would be the limited accessibility of polymer DBCO groups, which may be buried within the polymer coil because of hydrophobic effects. As shown in Fig. 2B, 19K-12DBCO polymers form rigid layers upon binding to Au-PEGN$_3$, suggesting a compact conformation. Furthermore, as shown in Fig. 3A, Au-PEGN$_3$ nanoclusters could not bind to pre-formed conjugates immobilized on the surface, whereas additional 19K-12DBCO polymers still could, even when the initial polymer was in excess. Similar results were observed for 92K-46DBCO (Fig. S15). This asymmetry implies that azide groups on nanoclusters are more accessible than the hydrophobic DBCO groups on the polymers, where the latter are a limiting factor slowing down the SPAAC reaction.

In summary, QCM-D analysis confirms that the bioorthogonal SPAAC reaction between azide-functionalized gold nanoclusters and DBCO-functionalized polymers in aqueous solution is highly specific and relatively slow. At the studied range of concentrations (1–10 μM), the reaction leads to nanocluster functionalization rather than formation of their network.

3.5. Optical properties of nanocluster/polymer conjugates

Changes in the optical properties of Au-PEGN$_3$ nanoclusters upon their mixing with 19K-12DBCO and 92K-46DBCO polymers were investigated in solution using UV-visible and photoluminescence (PL) spectroscopy (Fig. 4 and S16). The UV-visible spectra of mixtures, pre-incubated for 1 hour at a 10 : 1 polymer-to-nanocluster ratio, are shown in Fig. 4A and S15A, together with the spectra of each component alone. The overall shape of the absorbance spectrum of Au-PEGN$_3$ remained unchanged after conjugation with DBCO-functionalized polymers, indicating that the core structure and electronic properties of the nanocluster were preserved. A slight increase in absorbance intensity may indicate the presence of a minor fraction of nanocluster aggregates. This was further examined by TEM for the 19K-polymer system, revealing that the core size of the nanoclusters remained largely unaffected by conjugation with either 19K-12DBCO or 19K-24DBCO, even in the presence of a ten-fold excess of polymer (Fig. S17). These results confirm that the SPAAC reaction does not promote the formation of large-scale nanocluster assemblies at low concentration, in agreement with the QCM-D data (Fig. 3).

PL emission spectra recorded for Au-PEGN$_3$ before and after 1-hour incubation with a ten-fold excess of 19K-12DBCO (Fig. 4B) show a 1.7-fold increase in PL intensity and a 20 ± 2 nm blue shift of the emission peak (inset, Fig. 4B). Similar results were observed upon conjugation with 92K-46DBCO polymers: 1.8-fold PL enhancement with a blue shift of 18 ±

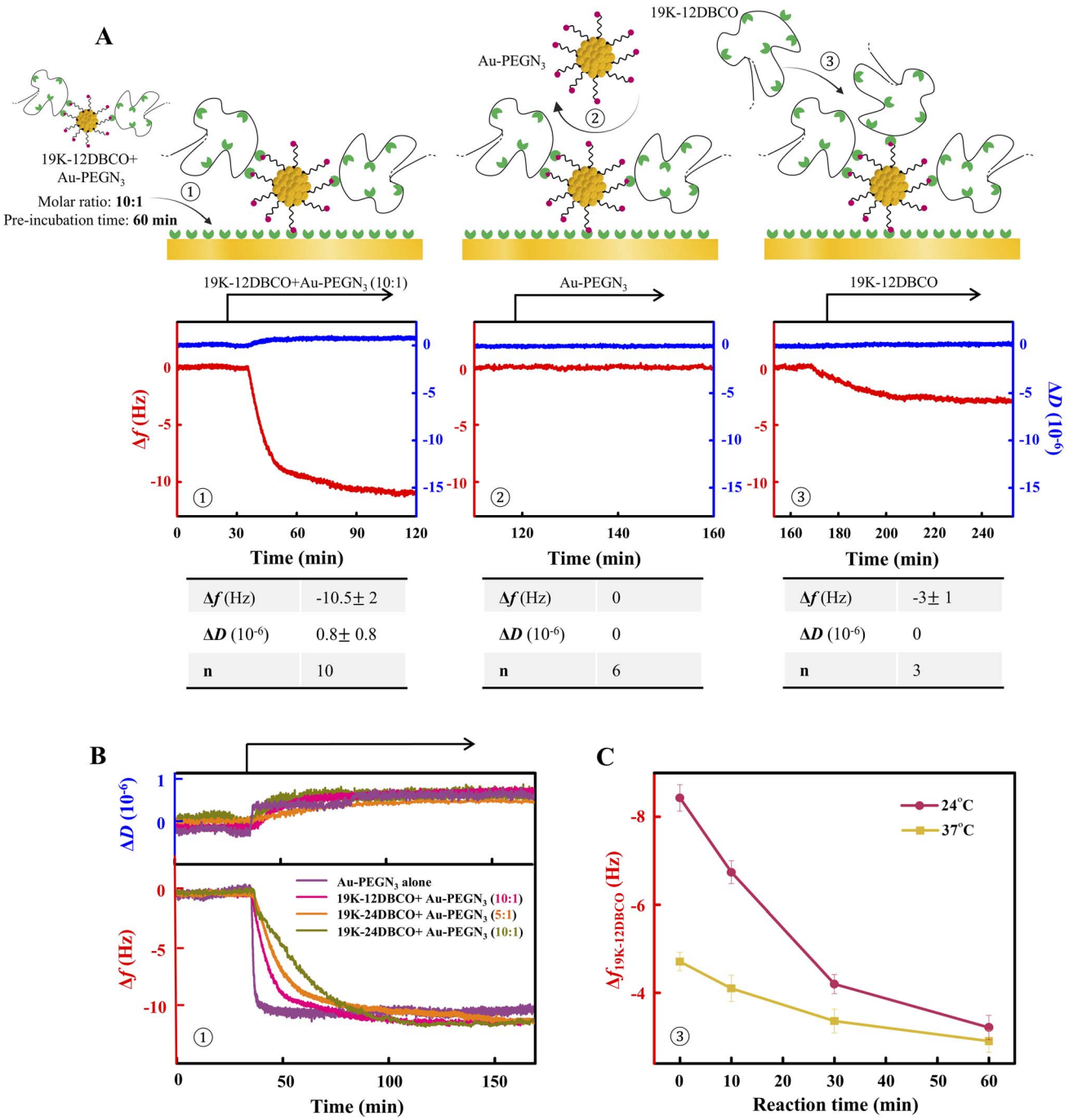

Fig. 3 Characterization of kinetics and stoichiometry of bioorthogonal conjugation using QCM-D. (A) Schematic representation of interactions studied on DBCO-coated surfaces and reflected in Δf (red) and ΔD (blue) shifts (overtone $i = 7$) during the injection of ① the mixture of 19K-12DBCO and Au-PEGN$_3$ (at a polymer : AuNC molar ratio of 10 : 1; [polymer] = 10 μM; [AuNC] = 1 μM), followed by the subsequent injection of ② Au-PEGN$_3$ (1 μM) and ③ 19K-12DBCO (10 μM). Values in the table represent the mean ± SEM from n measurements. The arrows at the top of the QCM-D profile indicate the start and incubation duration with each sample as specified, while a working buffer (PBS) was flushed over the sensor surface during the remaining periods. (B) The overlay of QCM-D profiles obtained during the exposure of DBCO-coated surfaces to the Au-PEGN$_3$: 19K-12DBCO mixtures at different ratios, with a pre-mixing time of 60 min. (C) Frequency shifts obtained at 24 and 37 °C during the injection of 19K-12DBCO (10 μM) (in step ③) to surface pre-exposed to the mixtures of Au-PEGN$_3$ and 19K-12DBCO (in step ①) while varying the time of their pre-mixing.

2 nm (Fig. S16B). The observed blue shift is likely due to modifications in the nanocluster surface chemistry following polymer conjugation, which can alter the electronic energy levels and surface trap states.[40,41] Further experiments were conducted by varying the concentration of Au-PEGN$_3$ while keeping the polymer concentration constant (10 μM). The

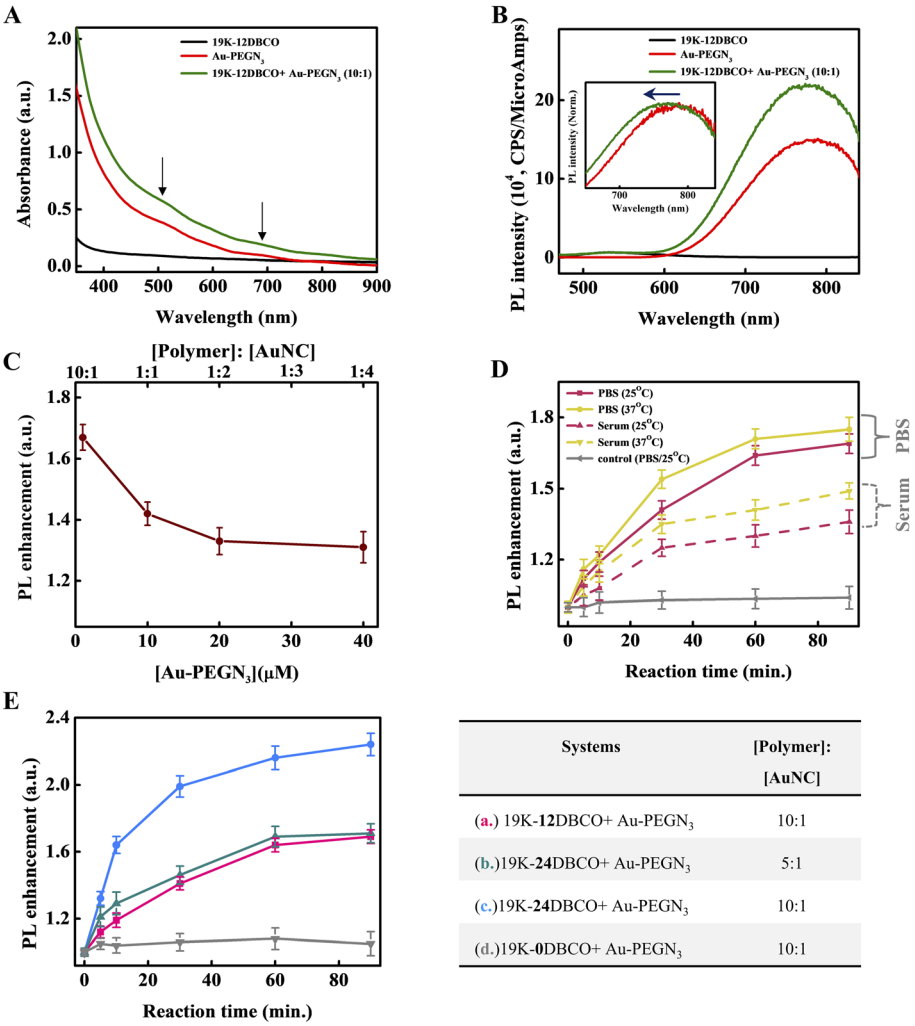

Systems	[Polymer]: [AuNC]
(a.) 19K-**12**DBCO+ Au-PEGN$_3$	10:1
(b.)19K-**24**DBCO+ Au-PEGN$_3$	5:1
(c.)19K-**24**DBCO+ Au-PEGN$_3$	10:1
(d.)19K-**0**DBCO+ Au-PEGN$_3$	10:1

Fig. 4 Optical properties of nanocluster/polymer conjugates. The characteristic (A) absorbance and (B) PL emission spectra ($\lambda_{exc} = 450$ nm) of 19K-12DBCO (black), Au-PEGN$_3$ (red) and the mixture of 19K-12DBCO : Au-PEGN$_3$ at a 10 : 1 ratio (green) (concentrations of Au-PEGN$_3$ and 19K-12DBCO used are 1 and 10 μM, respectively). The inset in (B) shows the blue shift (~20 ± 2 nm, $n = 3$) of the PL emission maximum upon mixing Au-PEGN$_3$ with 19K-12DBCO. (C) PL enhancement recorded for Au-PEGN$_3$: 19K-12DBCO mixtures at different Au-PEGN$_3$ concentrations keeping 19K-12DBCO concentration fixed to 10 μM. Absorbance and PL emission experiments were done at 25 °C in PBS; all mixtures were pre-incubated for 1 hour. (D) PL enhancement recorded for the mixtures of 19K-12DBCO : Au-PEGN$_3$ at a 10 : 1 ratio as a function of pre-incubation time in PBS or DMEM with 10% serum at 25 (pink) or 37 °C (yellow); [Au-PEGN$_3$] = 1 μM, [19K-12DBCO] = 10 μM, number of experiments averaged = 2. Control system based on Au-PEGOCH$_3$ is shown in gray. (E) The PL enhancement for the mixtures of 19K-12DBCO : Au-PEGN$_3$ at tunable ratios and DBCO density plotted as a function of their pre-incubation time; experiments are done at 25 °C in PBS (number of experiments averaged = 2). A table summarizing the studied mixtures is shown next to the graph.

dependence of PL enhancement on nanocluster concentration and on the nanocluster-to-polymer ratio is shown in Fig. 4C for 19K-12DBCO and in Fig. S16C for 92K-46DBCO. Regardless of polymer molecular weight, maximum PL enhancement was consistently achieved under conditions of polymer excess. This trend was reproduced in complementary experiments where polymer concentration was varied while keeping the nanocluster concentration fixed (Fig. S18).

Varying the pre-incubation time confirmed the QCM-D observations: the reaction proceeds slowly, with no plateau in PL intensity reached even after 1 hour (Fig. 4D and S15D). An increase in temperature from 25 to 37 °C resulted in a noticeable enhancement in PL intensity, consistent with the higher conjugation kinetics observed in QCM-D experiments under the same conditions (Fig. 3). The influence of the surrounding medium was also examined by comparing PL responses in PBS and in DMEM supplemented with 10% serum. PL enhancement was comparable in PBS and DMEM, but significantly lower in DMEM containing 10% serum (Fig. 4D and S19). The results demonstrate that bioorthogonal conjugation can occur in biologically relevant environments. The lower PL enhancement observed in the presence of serum likely reflects non-specific interactions with biomolecules, which may alter the local environment around the nanoclusters or interfere with the conjugation efficiency.

As for the origin of the PL enhancement, the combined QCM-D, UV-visible, and TEM data suggest that the observed increase arises from surface functionalization of individual

nanoclusters rather than from the formation of assemblies. The enhancement is thus attributed to changes in the nanocluster's nano-environment,[42–44] particularly to the presence of a polymer inter-layer between the nanocluster surface and the surrounding solution that could lead to the rigidification of the AuNC ligand shell, resulting in the suppression of non-radiative pathways. This mechanism is supported by previous studies showing that ligand rigidification has a stronger effect on emission properties than dielectric changes alone.[42,45] Control experiments using Au-PEGOCH$_3$ under identical conditions showed negligible PL changes, confirming that the enhancement is specific to azide–DBCO conjugation and does not occur because of the presence of free polymers in solution (Fig. 4D and S15D, grey curves). This conclusion is further supported by the observation that higher DBCO density in the polymer leads to stronger PL enhancement (Fig. 4E and S15E). This effect may be linked to faster SPAAC kinetics, resulting in denser polymer coverage around nanoclusters, as well as to an increase in local hydrophobicity due to the greater number of DBCO units, both in line with the QCM-D results presented in Fig. 3C.

4. Conclusion

In summary, this study reveals that the bioorthogonal SPAAC reaction between azide-functionalized gold nanoclusters and DBCO-functionalized polymers in aqueous solution is highly specific but proceeds relatively slowly under diluted conditions. Comprehensive characterization, both on the surface using a QCM-D and in solution *via* PL spectroscopy, indicates that the reaction primarily involves individual nanoclusters, resulting in surface functionalization rather than the formation of large-scale networks. These observations are further corroborated by UV-visible spectroscopy and TEM analyses. Faster kinetics were observed in the presence of an excess of polymer, with higher DBCO density, and at elevated temperatures. Importantly, the reaction can also be carried out under conditions that mimic biological environments. This work provides a framework for the efficient SPAAC conjugation between AuNCs and polymers and establishes a robust experimental platform for probing the assembly and behavior of nano-conjugates. Furthermore, the obtained insights are applicable to other functional nano-objects, such as nanoparticles or liposomes, providing strategies to optimize SPAAC kinetics, specificity and photophysical properties across diverse nano-material systems.

Author contributions

The manuscript was written through contributions of all authors. All authors have given approval to the final version of the manuscript.

Conflicts of interest

The authors declare no conflict of interest.

Data availability

All the raw data related to the physico-chemical, analytical, optical characterizations will be available upon requested to the two corresponding authors: Dr Xavier Le Guével (Xavier.le-guevel@univ-grenoble-alpes.fr) and Dr Galina Dubacheva (galina.-dubacheva@univ-grenoble-alpes.fr).

Supplementary information: Additional physico-chemical characterization studies of polymers, nanoclusters and their conjugates. See DOI: **https://doi.org/10.1039/d5na00687b**.

Acknowledgements

XLG: SIREN "ANR-20-CE92-0039-01", NAnoGOLD "ANR-22-CE29-0022", XLG, GVD, AF, JLC, DB: ANR SEQUOIA "ANR-22-CE18-0006". We thank Jean-luc Puteaux (CERMAV, Grenoble) for performing HRTEM experiments and Muriel Jourdan (DCM, Grenoble) and Romain Sanahuges (ICMG platform, Grenoble) for assistance with NMR experiments and Laure Fort (ICMG platform, Grenoble) for assistance with MS measurements. We also acknowledge Agnès Crépet (IMP, Lyon) for SEC-MALLS and Carlos Fernandez-De Alba (IMP, Lyon) for DOSY NMR experiments, as well as the liquid chromatography, NMR platforms of ICL (Lyon) and UAR2045 CSpec-LaDoua for their expertise and technical support.

References

1 J. M. Baskin, J. A. Prescher, S. T. Laughlin, N. J. Agard, P. V. Chang, I. A. Miller, A. Lo, J. A. Codelli and C. R. Bertozzi, *Proc. Natl. Acad. Sci. U. S. A.*, 2007, **104**, 16793–16797.
2 S. L. Scinto, D. A. Bilodeau, R. Hincapie, W. Lee, S. S. Nguyen, M. Xu, C. W. am Ende, M. G. Finn, K. Lang, Q. Lin, J. P. Pezacki, J. A. Prescher, M. S. Robillard and J. M. Fox, *Nat. Rev. Methods Primers*, 2021, **1**, 30.
3 M. M. A. Mitry, F. Greco and H. M. I. Osborn, *Chem.–Eur. J.*, 2023, **29**, e202203942.
4 W. Yi, P. Xiao, X. Liu, Z. Zhao, X. Sun, J. Wang, L. Zhou, G. Wang, H. Cao, D. Wang and Y. Li, *Signal Transduction Targeted Ther.*, 2022, **7**, 386.
5 J. Yang, B. Zhu and C. Ran, *Chem. Biomed. Imaging*, 2023, **1**, 434–447.
6 N. Sharma, W. Mohammad, X. Le Guével and A. Shanavas, *Chem. Biomed. Imaging*, 2024, **2**, 462–480.
7 S. Mussa Farkhani, P. Dehghankelishadi, A. Refaat, D. Veerasikku Gopal, A. Cifuentes-Rius and N. H. Voelcker, *Prog. Mater. Sci.*, 2024, **142**, 101229.
8 M. París Ogáyar, Z. Ayed, V. Josserand, M. Henry, Á. Artiga, L. Didonè, M. Granado, A. Serrano, A. Espinosa, X. Le Guével and D. Jaque, *ACS Nano*, 2025, **19**, 7821–7834.
9 X. Le Guével, K. D. Wegner, C. Würth, V. A. Baulin, B. Musnier, V. Josserand, U. Resch-Genger and J.-l. Coll, *Chem. Commun.*, 2022, **58**, 2967–2970.
10 Z. Yu, B. Musnier, K. D. Wegner, M. Henry, B. Chovelon, A. Desroches-Castan, A. Fertin, U. Resch-Genger, S. Bailly,

J.-L. Coll, Y. Usson, v. josserand and X. Le Guével, *ACS Nano*, 2020, **14**, 4973–4981.
11 A. Baghdasaryan and H. Dai, *Chem. Rev.*, 2025, **125**, 5195–5227.
12 C. N. Loynachan, A. P. Soleimany, J. S. Dudani, Y. Lin, A. Najer, A. Bekdemir, Q. Chen, S. N. Bhatia and M. M. Stevens, *Nat. Nanotechnol.*, 2019, **14**, 883–890.
13 E. Porret, X. Le Guével and J. L. Coll, *J. Mater. Chem. B*, 2020, **8**, 2216–2232.
14 K. He, C. Hu, Y.-F. Ding, W. Cai, D. Huang, L. Mo, J. Liu and R. Wang, *Nano Today*, 2024, **56**, 102245.
15 Z. Pang, W. Yan, J. Yang, Q. Li, Y. Guo, D. Zhou and X. Jiang, *ACS Nano*, 2022, **16**, 16019–16037.
16 M. F. Matus and H. Häkkinen, *Bioconjugate Chem.*, 2024, **35**, 1481–1490.
17 Z. Yang, X. Yang, Y. Guo and H. Kawasaki, *ACS Appl. Bio Mater.*, 2023, **6**, 4504–4517.
18 D. Luo, X. Wang, S. Zeng, G. Ramamurthy, C. Burda and J. P. Basilion, *Small*, 2019, **15**, 1900968.
19 G. Liang, X. Jin, S. Zhang and D. Xing, *Biomaterials*, 2017, **144**, 95–104.
20 S. Moro, M. Omrani, S. Erbek, M. Jourdan, C. I. Vandekerckhove, C. Nogier, L. Vanwonterghem, M.-C. Molina, P. Bernadó, A. Thureau, J.-L. Coll, O. Renaudet, X. Le Guével and V. Faure, *Small Sci.*, 2024, **5**, 2400156.
21 M. Broekgaarden, A.-L. Bulin, E. Porret, B. Musnier, B. Chovelon, c. ravelet, L. Sancey, H. Elleaume, P. Hainaut, J.-L. Coll and X. Le Guevel, *Nanoscale*, 2020, **12**, 6959–6963.
22 M. F. Matus and H. Häkkinen, *Nat. Rev. Mater.*, 2023, **8**, 372–389.
23 L. Haye, P. I. Diriwari, A. Alhalabi, T. Gallavardin, A. Combes, A. S. Klymchenko, N. Hildebrandt, X. Le Guével and A. Reisch, *Adv. Opt. Mater.*, 2022, **11**, 2201474.
24 B. Casteleiro, F. Da Cruz-Boisson, P. Alcouffe, S. N. Pinto, J. M. Gaspar Martinho, M.-T. Charreyre, J. P. S. Farinha and A. Favier, *ACS Appl. Nano Mater.*, 2023, **6**, 11689–11698.
25 N. N. M. Adnan, S. Ahmad, R. P. Kuchel and C. Boyer, *Mater. Chem. Front.*, 2017, **1**, 80–90.
26 V. G. Deepagan, M. N. Leiske, N. L. Fletcher, D. Rudd, T. Tieu, N. Kirkwood, K. J. Thurecht, K. Kempe, N. H. Voelcker and A. Cifuentes-Rius, *Nano Lett.*, 2021, **21**, 476–484.
27 S. B. van der Meer, K. Loza, K. Wey, M. Heggen, C. Beuck, P. Bayer and M. Epple, *Langmuir*, 2019, **35**, 7191–7204.
28 P. N. Gunawardene, J. F. Corrigan and M. S. Workentin, *J. Am. Chem. Soc.*, 2019, **141**, 11781–11785.
29 D. Duret, A. Grassin, M. Henry, T. Jacquet, F. Thoreau, S. Denis-Quanquin, J.-L. Coll, D. Boturyn, A. Favier and M.-T. Charreyre, *Bioconjugate Chem.*, 2017, **28**, 2241–2245.
30 A. Favier, F. D'Agosto, M.-T. Charreyre and C. Pichot, *Polymer*, 2004, **45**, 7821–7830.
31 F. Aldeek, M. A. H. Muhammed, G. Palui, N. Zhan and H. Mattoussi, *ACS Nano*, 2013, **7**, 2509–2521.
32 D. Mishra, F. Aldeek, E. Lochner, G. Palui, B. Zeng, S. Mackowski and H. Mattoussi, *Langmuir*, 2016, **32**, 6445–6458.
33 B. Chabaud, H. Bonnet, R. Lartia, A. Van Der Heyden, R. Auzély-Velty, D. Boturyn, L. Coche-Guérente and G. V. Dubacheva, *Langmuir*, 2024, **40**, 4646–4660.
34 G. V. Dubacheva, C. Araya-Callis, A. Geert Volbeda, M. Fairhead, J. Codée, M. Howarth and R. P. Richter, *J. Am. Chem. Soc.*, 2017, **139**, 4157–4167.
35 L. Shang, N. Azadfar, F. Stockmar, W. Send, V. Trouillet, M. Bruns, D. Gerthsen and G. U. Nienhaus, *Small*, 2011, **7**, 2614–2620.
36 H. Qian, M. Zhu, Z. Wu and R. Jin, *Acc. Chem. Res.*, 2012, **45**, 1470–1479.
37 T. D. Fernández, J. R. Pearson, M. P. Leal, M. J. Torres, M. Blanca, C. Mayorga and X. Le Guével, *Biomaterials*, 2015, **43**, 1–12.
38 E. Oh, J. B. Delehanty, L. D. Field, A. J. Mäkinen, R. Goswami, A. L. Huston and I. L. Medintz, *Chem. Mater.*, 2016, **28**, 8676–8688.
39 G. V. Dubacheva, T. Curk, D. Frenkel and R. P. Richter, *J. Am. Chem. Soc.*, 2019, **141**, 2577–2588.
40 A. Yahia-Ammar, D. Sierra, F. Mérola, N. Hildebrandt and X. Le Guével, *ACS Nano*, 2016, **10**, 2591–2599.
41 G. Zhang, B. Fang, J. Peng, S. Deng, L. Hu and W. Lai, *Chem. Eng. J.*, 2025, **503**, 158294.
42 K. Pyo, V. D. Thanthirige, K. Kwak, P. Pandurangan, G. Ramakrishna and D. Lee, *J. Am. Chem. Soc.*, 2015, **137**, 8244–8250.
43 S. Zhu, X. Wang, Y. Cong and L. Li, *ACS Omega*, 2020, **5**, 22702–22707.
44 Y. Huang, X. Han, L. Wang and R. Pei, *Adv. Opt. Mater.*, 2024, **12**, 2400078.
45 X. Luo, J. Kong, H. Xiao, D. Sang, K. He, M. Zhou and J. Liu, *Angew. Chem., Int. Ed.*, 2024, **63**, e202404129.

